FIBER MODEL FOR REINFORCED CONCRETE WALLS

J. Vásquez(1), J.C. de la Llera(2), M. Hube(3)

(1) Research assistant, National Research Center for Integrated Natural Disaster Management CIGIDEN CONICYT/FONDAP/15110017 and Pontificia Universidad Católica de Chile, jorge.vasquez@cigiden.cl
(2) Professor, National Research Center for Integrated Natural Disaster Management CIGIDEN CONICYT/FONDAP/15110017 and Department of Structural and Geotechnical Engineering, Pontificia Universidad Católica de Chile, jcllera@ing.puc.cl
(3) Associate professor, National Research Center for Integrated Natural Disaster Management CIGIDEN CONICYT/FONDAP/15110017 and Department of Structural and Geotechnical Engineering, Pontificia Universidad Católica de Chile, mhube@ing.puc.cl

Abstract

Due to the taller reinforced concrete (RC) buildings that have been constructed in recent years, shear walls at lower levels are subjected to higher axial loads and bending moments. Although complex finite element inelastic models for shear walls can effectively couple several effects at the stress-strain level, they are computationally demanding, and hence robust and computationally efficient models are necessary to quickly assess the earthquake performance of these buildings. Herein, a pure two-node fiber element model that takes into account axial and bending components only, was modified to produce objective results under common loading conditions of the walls identified in Chilean buildings, i.e., high axial loads with linear bending moment variation between floors. A regularization is required to predict results independent of the element size and a shear model based on the modified compression field theory was added into this element to simulate the behavior of shear walls adequately. This investigation focuses in the formulation of the proposed model, its validation with experimental tests reported in the literature, and its application to actual RC walls of buildings. It was found that the steel stress-strain constitutive behavior, the inclusion of shear deformation, and the strain penetration effects played an important role in reproducing the experimental behavior of walls. Additionally, the proposed model is able to predict the observed collapse mechanisms of walls in buildings damaged during the 2010 earthquake. Since the element is capable of reproducing experimental tests and earthquake response, and since it is numerically more efficient than other approaches, its use for complete 3D inelastic dynamic analysis of buildings is promising.

Keywords: reinforced concrete, fiber model, wall, regularization

1. Introduction

Reinforced concrete (RC) walls are of common use in seismic countries since they have shown a good performance in previous massive earthquakes such as the 1985, Chile earthquake [1]. Following this success, most residential buildings in Chile are still based on RC walls deployed in plan as a fish-bone like structure. During the 2010 Chile earthquake most of RC wall buildings behaved well, and around 2% of buildings taller than 5 stories suffered severe damage [2] including one complete collapse [3]. A common observed damage consisted of concrete crushing, and buckling and fracture of vertical reinforcement localized in walls at the lower levels of buildings. This kind of damage can be attributed to: (1) taller buildings producing higher axial and shear loads on walls; (2) the presence of irregularities along the height of the building (3) poor wall confinement; and (4) thinner walls.

Analyzing three-dimensional inelastic models of such buildings with hundreds of thousands degrees of freedom is still a difficult task due to the huge computational cost and validation of inelastic models. However, since damage was localized in the first stories of buildings, it is reasonable to concentrate nonlinearities only in critical elements that control the inelastic response. Additionally, desired characteristics of inelastic models are: (1) responses have to be objective, i.e, they should not be mesh dependent; (2) the computational cost should be minimal while keeping adequate accuracy, and (3) the definition of parameters should not need calibration.

Among the numerous RC concrete models, force-based fiber elements (FFE) are a good choice compared to other modeling approach such as 2D/3D shell finite elements, because FFE are simple, robust and use limited amount of memory. However, two critical issues of FFE to model RC walls are: (1) lack of coupling between shear and axial-bending behavior, and (2) numerical localization of deformations at the most demanded section, which is induced when softening materials are used. To solve the first issue, two major approaches have been taken. The first one is to impose equilibrium in the transverse direction of the wall at the local level [4, 5, 6] adding one level of iteration when determining the fiber's state, thus increasing the computational effort. The second approach combines flexural and shear sub-elements, and does not impose transverse equilibrium locally [7, 8]. This latter approach is less computationally expensive than the first approach but the coupling effect are weaker.

For the numerical localization issue, two approaches have been proposed in the literature. The first one is to modify the integration scheme such that the integration length associated to the end points matches the desired plastic hinge length [9, 10]. The second one is to modify the strain-stress curves by keeping the post peak fracture energy constant, making the constitutive relationship mesh dependent [11, 12].

This paper presents a force based wall element (FWE) composed of a FFE including a modified regularization technique, coupled to a shear model at the element level, and its application to one structural element and to complex walls within buildings.

2. Formulation of the element

The FWE consist of two sub-elements connected in parallel as shown in Figure 1a: (1) a fiber element that accounts for the axial and bending behavior, and (2) a pure shear element. Torsion in the element is assumed to remain linear-elastic. The main equations are presented here and the detailed formulation can be found elsewhere [13]. The three equations imposed in the flexibility method are: (1) equilibrium, (2) force-deformation constitutive relationship, and (3) kinematics. In order to apply these equations, a cantilever element was chosen as the basic system. The equilibrium equation reads

$$\boldsymbol{D}(x) = \boldsymbol{b}(x)\boldsymbol{Q} \tag{1}$$

Where $\boldsymbol{Q} = \left[N, M_y, M_z, V_y, V_z, T\right]^T$ is the total nodal forces at the free node, which components are the axial force N, the bending moments M_y and M_z about the y and z axes, the shear forces V_y and V_z along the y and z axes, and the torsional moment T. $\boldsymbol{D}(x) = \left[N(x), M_y(x), M_Z(x), V_y(x), V_z(x), T(x)\right]^T$ is the section forces at every point along the longitudinal axis x of the element of length L, and $\boldsymbol{b}(x)$ is the equilibrium matrix. The force-deformation relationship relates the section forces $\boldsymbol{D}(x)$ with the section deformations

$\boldsymbol{d}(x) = [\varepsilon(x), \kappa_y(x), \kappa_z(x), \gamma_{xy}(x), \gamma_{xz}(x), \gamma_t(x)]^T$ where ε, κ and γ are conjugate quantities (in work terms) to $\boldsymbol{D}(x)$ and denote axial deformation, curvature, and angular distortion, respectively. The incremental force-deformation equation reads

$$\Delta\boldsymbol{d}(x) = \boldsymbol{f}(x)\Delta\boldsymbol{D}(x) \tag{2}$$

Where $\boldsymbol{f}(x)$ is the complete section flexibility matrix defined as:

$$\boldsymbol{f}(x) = \begin{bmatrix} \boldsymbol{f}_{AF\,3x3} & \boldsymbol{0}_{3x1} & \boldsymbol{0}_{3x1} & \boldsymbol{0}_{3x1} \\ \boldsymbol{0}_{1x3} & f_{Sy} & 0 & 0 \\ \boldsymbol{0}_{1x3} & 0 & f_{Sz} & 0 \\ \boldsymbol{0}_{1x3} & 0 & 0 & f_T \end{bmatrix} \tag{3}$$

and $\boldsymbol{f}_{AF}$ is the section flexibility matrix due to the axial and bending component; f_{S_y}, f_{S_z}, and f_T are the section shear flexibilities in the y-, z-, and torsional directions, respectively. In this formulation, the axial and bending behavior is coupled at the section level, as opposed to the shear and torsion behavior.
Finally, after applying the kinematic equation through the complementary virtual work principle, in combination with Eq. (1) and Eq. (2), one gets:

$$\boldsymbol{F}\Delta\boldsymbol{Q} = \Delta\boldsymbol{q} \tag{4}$$

Where $\Delta\boldsymbol{q}$ is the increment of the element displacement vector, and $\boldsymbol{F} = \int_0^L \boldsymbol{b}(x)^T\boldsymbol{f}(x)\boldsymbol{b}\,(x)dx$ is the element flexibility matrix. The term $\boldsymbol{b}(x)^T\boldsymbol{f}(x)\boldsymbol{b}\,(x)$ is responsible of coupling shear and the axial and bending component as in Timoshenko beam theory, keeping torsion completely uncoupled.

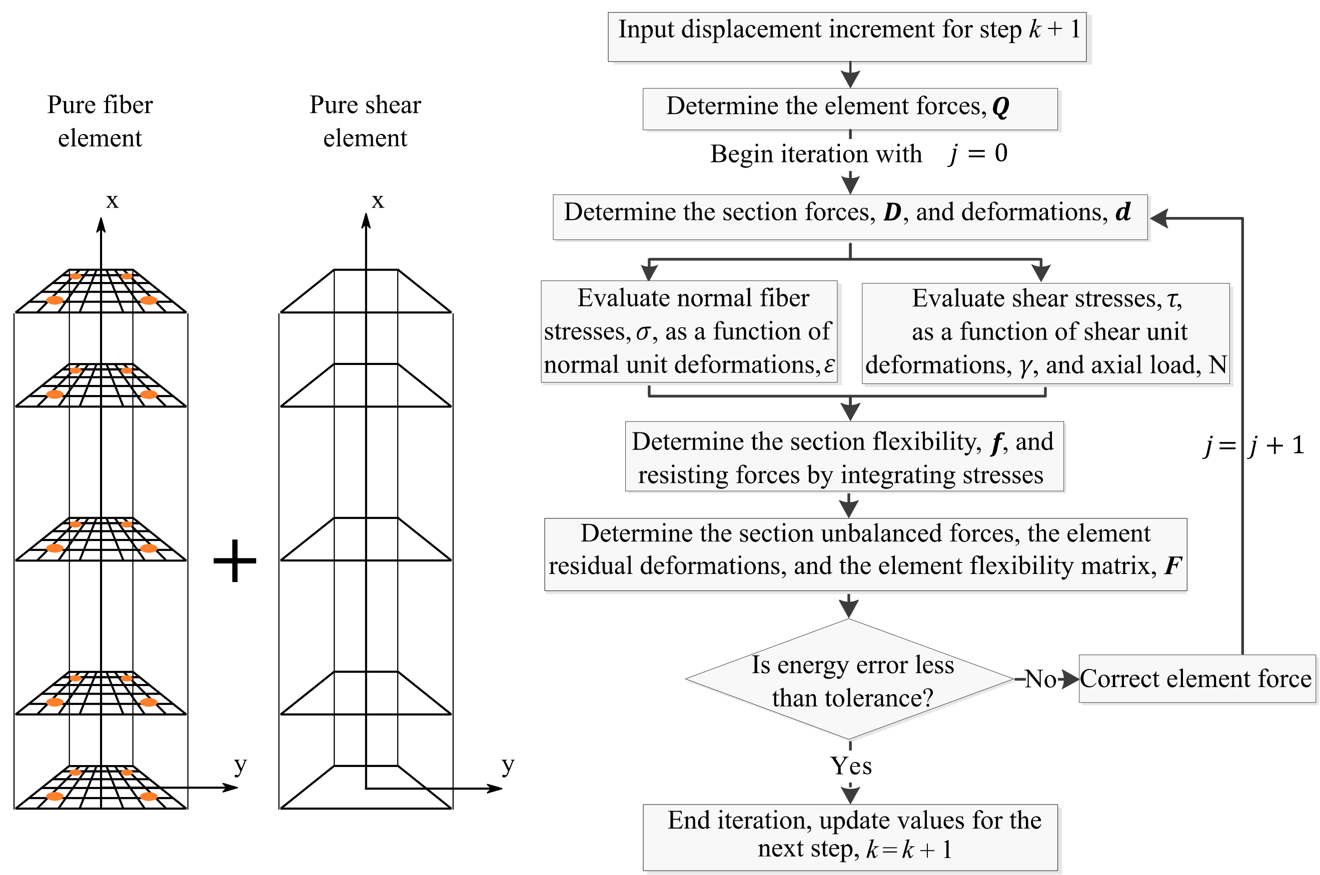

a) b)

Fig. 1 – Internal operation of FWE: (a) mechanical behavior, and (b) numeric procedure to determine the element state.

To integrate $\boldsymbol{F}$ and to compute the resisting forces $\boldsymbol{Q}$, all variables depending on x are evaluated at quadrature points along the longitudinal axis of the wall and then summed over with the corresponding weights. Locations and weights are given by the Gauss-Lobatto integration scheme, which has the advantage of including points at the edge of the element, where demands are higher under absence of forces along the element. Since FWE is forced based, an iterative procedure is needed to compute element forces and stiffness for a given nodal displacement, as shown schematically in Figure 1b. The complete algorithm can be found elsewhere [13].

2.1 Axial and bending behavior: Fiber model

The axial and bending behavior are modeled using a FFE proposed elsewhere [14], where perfect bond between steel and concrete is assumed. Shown in Figure 2 is the use of this model in the FWE with fibers of two kinds: concrete, and steel. The constitutive relationship of concrete fibers use the well-known Kent & Park model and tension stress is neglected. On the other hand, the steel constitutive curve is based on [15], that includes strain hardening, Bauschinger effect, and bar buckling, and the softening branch depends on the slenderness of the bars. Further details can be found elsewhere [13].

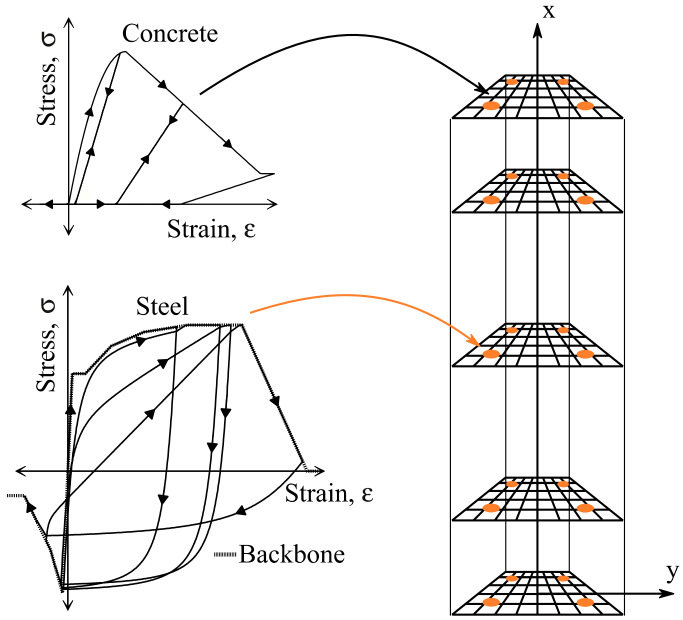

Fig. 2 – Fiber model of restrained element with concrete and steel fibers

2.2 Shear component

As seen in Figure 1a, shear deformations are included using a pure shear sub-element developed earlier [13] whose constitutive relationship is shown in Figure 3a and 3b. This constitutive is assumed to be uniform along the cross section, as in Timoshenko beam theory, and it is used independently in both directions of the wall. A typical macro model with no shear failure consists of two points: the cracking point (γ_{cr}, τ_{cr}) and the yielding point (γ_y, τ_y), which represents the peak shear strength (Figure 3a). However, in a bending-compression dominant behavior, the yielding point in this curve is not reached, and failure begins at $(\gamma_{flex}, \tau_{flex})$ driven by the bending-compression failure. After this point, the section degrades until it reaches complete failure (γ_f, τ_f). The first portion of the shear constitute curve is linear elastic with shear stiffness G=0.4E_c, where E_c is the modulus of elasticity of concrete. After (γ_{cr}, τ_{cr}), the cracked shear stiffness is estimated using the modified compression field theory (MCFT) and due to lack of data, the softening stiffness G_{soft} has been assumed to be -0.4E_c. Finally, the $\tau - \gamma$ curve is modified as axial load varies, as shown in Figure 3b. For this implementation, the backbone curve is described as a function of the axial load by using the MCFT, and the shear strength increases as the axial load increases (se Figure 3b). More details are available elsewhere [13].

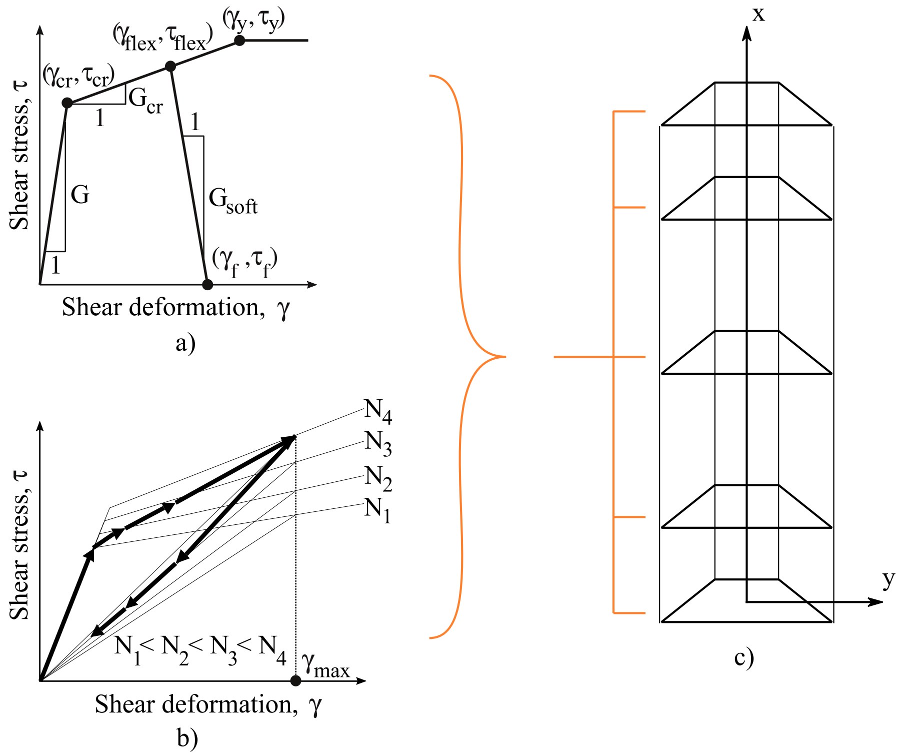

Fig. 3 – Shear model coupled with axial load.

3. Objectiveness in the global response

Experimentally, when softening material are used, deformations localize in a limited region in the most demanded zone. This phenomenon is known as localization, and is characterized by large deformations and concentration of damage. When subjected to compression, concrete and steel soften after reaching maximum strength due to crushing and buckling respectively. For this reason, RC walls subjected to bending and compression present a localized behavior forming the well-known plastic hinge. A localized behavior was also observed during the 2010 Chile earthquake, where buildings presented localized damage. Localization of deformations is also present in numerical analyses, particularly when using the FWE. If the predicted global response depends on the number of integration points used along the element, the response is not objective. In these cases, damage is localized in the most demanded element section, whose length, L_i, depends on the number of integration points: $L_i = w_i L$, where w_i is the weight resulting from the numerical integration scheme, and it's a function of the number of integration points.

The proposed regularization procedure proposed to obtain objective global responses was based on the modifications of the constitutive curves of concrete and steel [12, 14], and is denoted as energy regularization. However, a small yet profound modification is also needed to achieve objective responses for different load cases. The energy regularization method, first proposed elsewhere [14] modifies the softening branch of concrete and steel constitutive curves, as shown in Figure 4a$_2$, where the softening slope becomes steeper as the integration length becomes larger. However, localization starts when the global strength is reached, and not necessarily when fibers reach their local strength [13, 16]. In general, the global strength does not coincide with fibers strength, meaning that the modification of the softening slope should not start immediately when the fiber strength is reached, as in Figure 4a$_3$. In this study three situations where the original energy regularization method didn't produce objective results are: (1) high axial load ratios, say axial load to gross section area ratios, ALR>35%; (2) low axial load ratios, say ALR<5%; and (3) in regions of fairly constant bending moment, where section forces and deformations are similar at different integration points and any section may soften. Figure 4a shows schematically the regularization used for concrete in each row of the figure. To the right, Figure 4b and Figure 4c show numerical results after applying these regularization techniques for ALR=40% and ALR=0%

respectively. The wall used to produce these curves has a U-shaped cross section loaded along the Y direction (web direction) [17]. This wall is detailed in the next section.

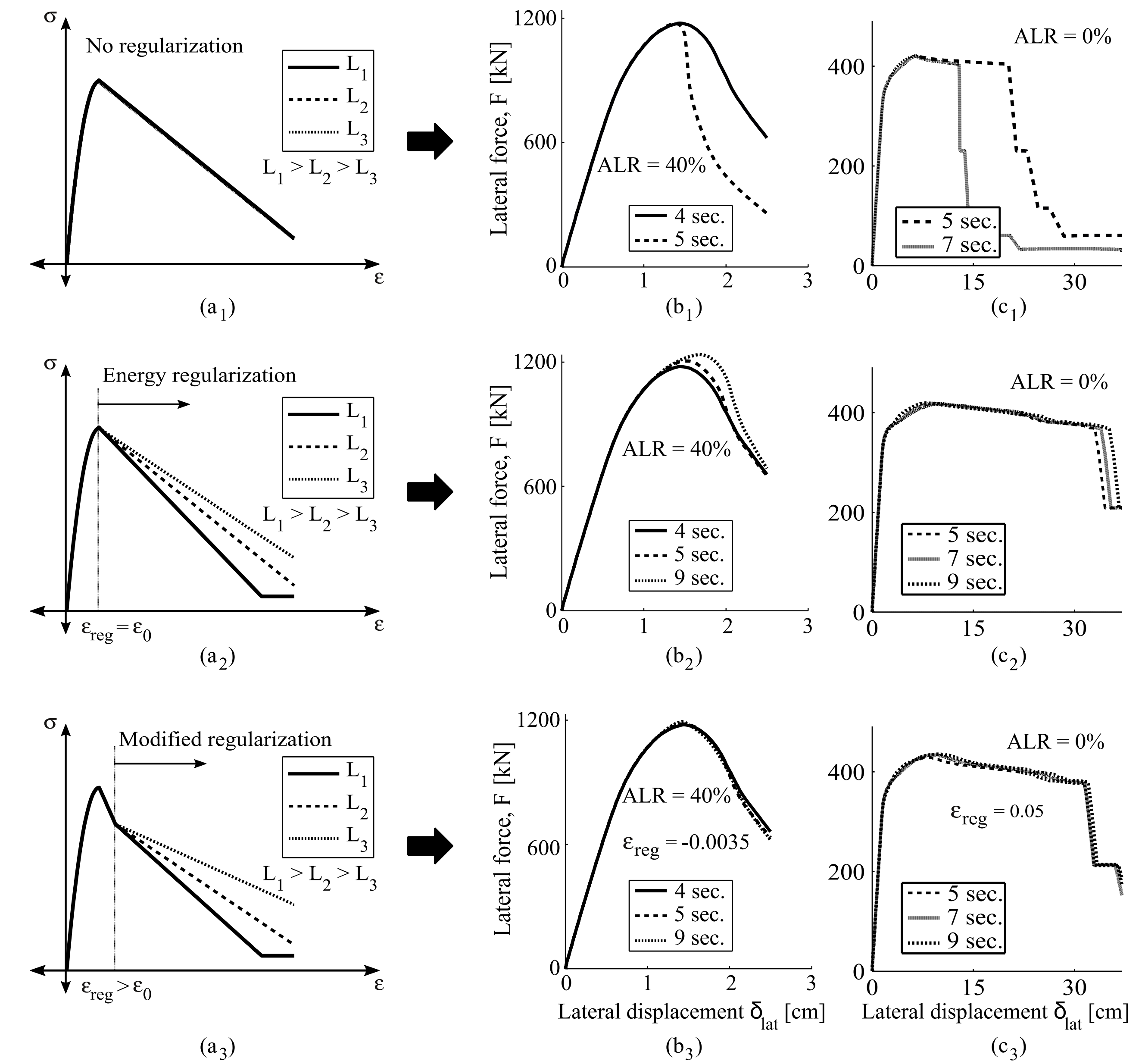

Fig. 4 – Comparison of different regularization techniques applied to a cantilever wall, using three regularization techniques: (a_1) no regularization, (a_2) energy regularization, and (a_3) proposed regularization, for two loading cases: (b) ALR=40%, and (c) for ALR = 0%. Compression is shown as positive in column (a)

Finally, as the shear model also has a softening region (Figure 3a), the same energy regularization approach is used. However, since the global shear strength always coincide with the section (local) shear strength, the modification shown in Figure 4a_3 is not require for the shear behavior. The detailed explanation can be found elsewhere [16].

4. Comparison against test results

The proposed model was tested using four different shear wall configurations in a cantilever-like loading configuration: a U-shaped wall denoted as USW1 [17]; a T-shaped wall denoted as NTW1 [18]; and two rectangular specimens WSH3 and WSH4 [19]. Table 1 summarizes some geometric properties of these walls. Parameters ρ_{web} and ρ_{flange} are the transverse steel ratio in the web and flange direction, respectively, and are computed by neglecting the additional reinforcement in boundary zones. The walls were tested under uniaxial or biaxial loading directions, Table 1. In case of USW1, the web is taken as the direction parallel to the two vertical elements of the U; in case of NTW1, the direction where the wall is longer; and for the rectangular walls, the web is taken as the main direction.

Table 2 summarizes the concrete mechanical properties of the selected walls. Parameter $f_c{}'$ is the compressive strength of plain concrete, and the concrete strain at this stress was assumed to be 0.002 for all walls; $f_{cc}{}'_{flange}$ is the concrete strength in confined zones along the flange and $f_{cc}{}'_{web}$ is the concrete strength in confined zones along the web. For the USW1 wall, the confined concrete zone in corners was labeled as $f_{cc}{}'_{flange}$. The same nomenclature applies for the crushing energies $G_{cc_{web}}$ and $G_{cc_{flange}}$ estimated using the average from the two different models [20] and [21]. Note that WSH4 does not have a confined zone as all the other specimens. The value G_c was calculated using $G_c = 8.8\sqrt{f_c{}'}$ with $f_c{}'$ in MPa and G_c in MPa-mm [22]. For strain penetration effects, the additional section at the base of the wall was modeled using Kent & Park model with a horizontal softening slope and the parameters for steel following the model found elsewhere [23], $R_e = 0.99$, $R_c = 1$, and $b = 0.4$.

Table 1. Geometric characteristics and axial load of the sample walls.

Wall	**Thickness [cm]**	**Area [m^2]**	**Shear span [m]**	ρ_{web}	ρ_{flange}	**ALR [%]**	**Loading direction**
NTW1	15.25	0.602	7.93	0.0062	0.0027	2.75	Biaxial
USW1	25	0.875	3.90	0.0053	0.0032	10.00	Uniaxial
WSH3	15	0.3	4.56	0.0025	-	5.30	Uniaxial
WSH4	15	0.3	4.56	0.0025	-	5.20	Uniaxial

Table 2. Concrete Mechanical properties of the walls.

Wall	$f_c{}'$ **[MPa]**	$f_{cc}{}'_{flange}$ **[MPa]**	$f_{cc}{}'_{web}$ **[MPa]**	G_c **[MPa-m]**	$G_{cc_{flange}}$ **[MPa-m]**	$G_{cc_{web}}$ **[MPa-m]**
NTW1	50.00	60.42	63.4	0.062	0.526	0.730
USW1	23.73	31.87	33.0	0.043	0.314	0.332
WSH3	39.20	-	46.1	0.057	-	0.350
WSH4	40.90	-	-	0.057	-	-

The comparison between the experimental and analytically predicted force-displacement curves of the cyclic tests of the four walls are shown in Figure 5. Plots a) and b) show the results for NTW1 along the web and flange directions respectively, where the general shape of the curves is estimated well, achieving similar maximum strength, ductility, and a reasonable unloading a reloading slopes. However, a more detailed comparison shows that, the analytical degradation in Figure 5a is larger than the experimental one. This larger degradation can be attributed to bond slip not accounted for in the model and the fixed end rotation could be underestimated for larger cycles due to the approximated modeling approach for this effect. Furthermore, the differences in the unloading paths in both directions can be attributed to the shear lag effect. Figure 5c shows a good estimation for wall USW1, except for the maximum strength, which is underestimated by 9%. Additionally, the model predicts more pinching than that of the experiment, because the model neglects the crack closure effects. Figures 5d and 5e show results for two rectangular walls, WSH3 and WSH4. Again, the general path is in agreement with experimental results, although the maximum strength is slightly underestimated (in about 2%) and there is a marked pinching in the analytical curves. However, it is worth noting that ductility is achieved adequately, and the abrupt loss in resistance occurs for similar displacement (errors less than 20%). The failure pattern of walls WSH3 and WSH4 is characterized by a crushed concrete and fracture of the outermost reinforcing bars due to high tensile strains in both the actual specimens and the analytical models.

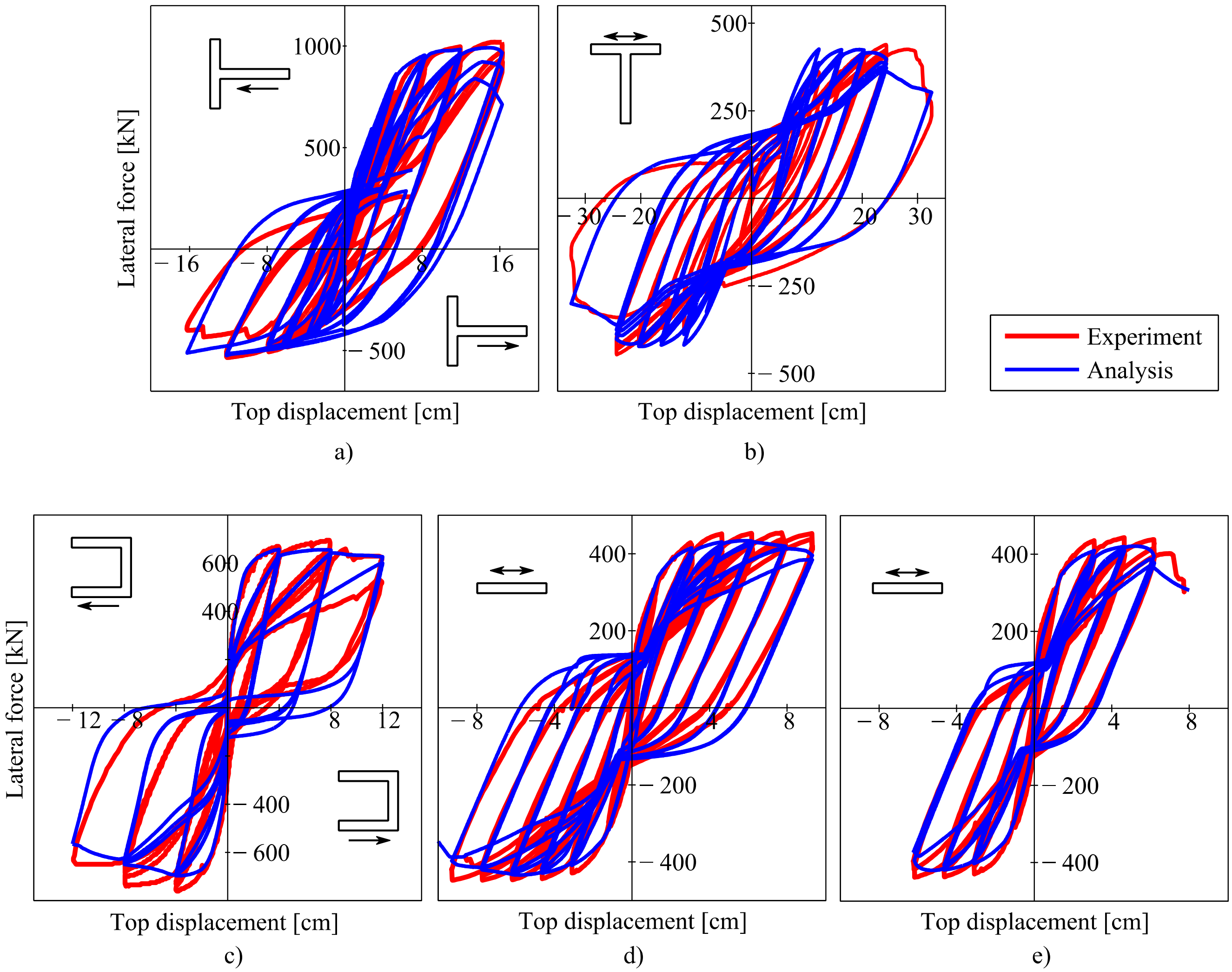

Fig. 5 – Comparison of the analytical and experimental force displacement responses for: a) NTW1 in web direction, b) NTW1 in flange direction, c) USW1 in flange direction, d) WSH3, and e) WSH4.

Figure 6 shows the shear component of three walls using available information in the literature. The first row of plots, Figure a-c, shows the fraction of shear displacements to total displacements in case of NTW1 (Figure 6a) and the fraction of shear displacements to flexural displacements for: b) WSH3, and c) WSH4. The second row of plots, Figure d-f, show the shear force-deformation curves after cyclic analyses of the most demanded section–the one closer to the foundation. From plots a) to c), it can be seen than errors are bigger than the total responses shown in Figure 5; however, the proposed model is clearly a better approximation that an elastic one, which is mainly because the proposed model includes a cracking zone where the section shear stiffness is greatly reduced (approximately it is reduced to 5% of the elastic one). Figure a) and d) shows a clear drawback of the shear model; it is a symmetric macro model uncoupled in both directions and from flexural effects. In the web direction, when flange is in tension the well-known shear lag effect [24] is produced and then the behavior is very different relative to the case when flange is in compression. Moreover, the lateral strength of the web when the flange is in tension doubles that of the flange in compression, and the proposed model does not capture this. The model assigns a symmetric rectangular shear area equal to the web of the wall in that direction.

Finally, although unloading and reloading paths are secant, this does not appear to have a big impact in the overall response.

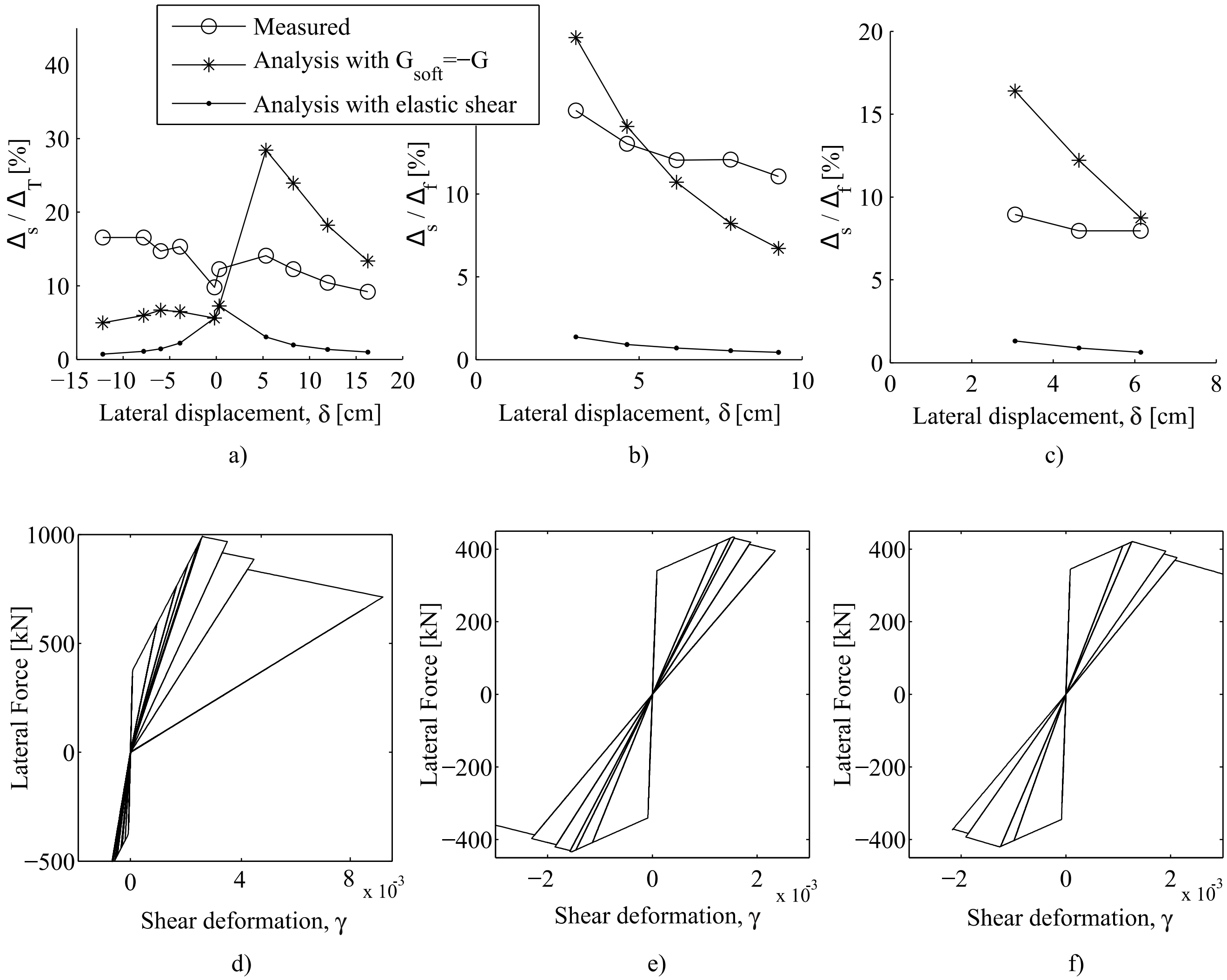

Fig. 6 – Comparison of shear responses between analytical and experimental results for: a) NTW1 in web direction, b) WSH3, and c) WSH4, and numerical cyclic shear responses for d) NTW1 in web direction, e) WSH3, and f) WSH4.

5. Modeling of walls with irregularities

Actual walls within buildings have irregularities in height. Their modeling is straightforward if we use shell elements; however, in the case of FWE that assumes plane sections remaining plane after deformation, special care must be taken in the critical zones. For simplicity, the elastic case is studied so that deformations using the FWE with elastic properties (E=22560 MPa) match those coming from shell element analysis using SAP2000 v15. The chosen T-shaped wall belongs to a building in Santiago, Chile, that suffered severe damage during the 2010 earthquake, and the detailing of the wall can be found elsewhere [25]. Figure 7a shows the 3D base model without the irregularity and the direction of the lateral force in the subsequent pushover analyses. Figure 7b shows its deformation when the wall is subjected to a lateral force of 687 kN at the top. The error of the displacements coming from the FWE model in comparison with the shell model is below 4% at all story levels (see Figure 7c). In this case the shear area used was the portion of the wall parallel to the force. Figure 7d shows the shell analysis of the cantilever wall with the irregularity near the bottom, where the length of the wall is 1.2m shorter in the first 6m of the wall in height. In the zoom up, the angle θ represents how the effective length of the FWE changes over the height of the wall, so that the hatched area at the corner represents no wall at all. As it is expected, using the same geometry than that of shell elements ($\theta = 90°$), the FWE model underestimates deformations (solid blue line in Figure7e), which is due to the plane section assumption that introduces a false stiffness around the irregularity; however, as the angle θ decreases, the effective length is reduced further away from the irregularity, and the model no longer overestimates deformations (dashed lines).

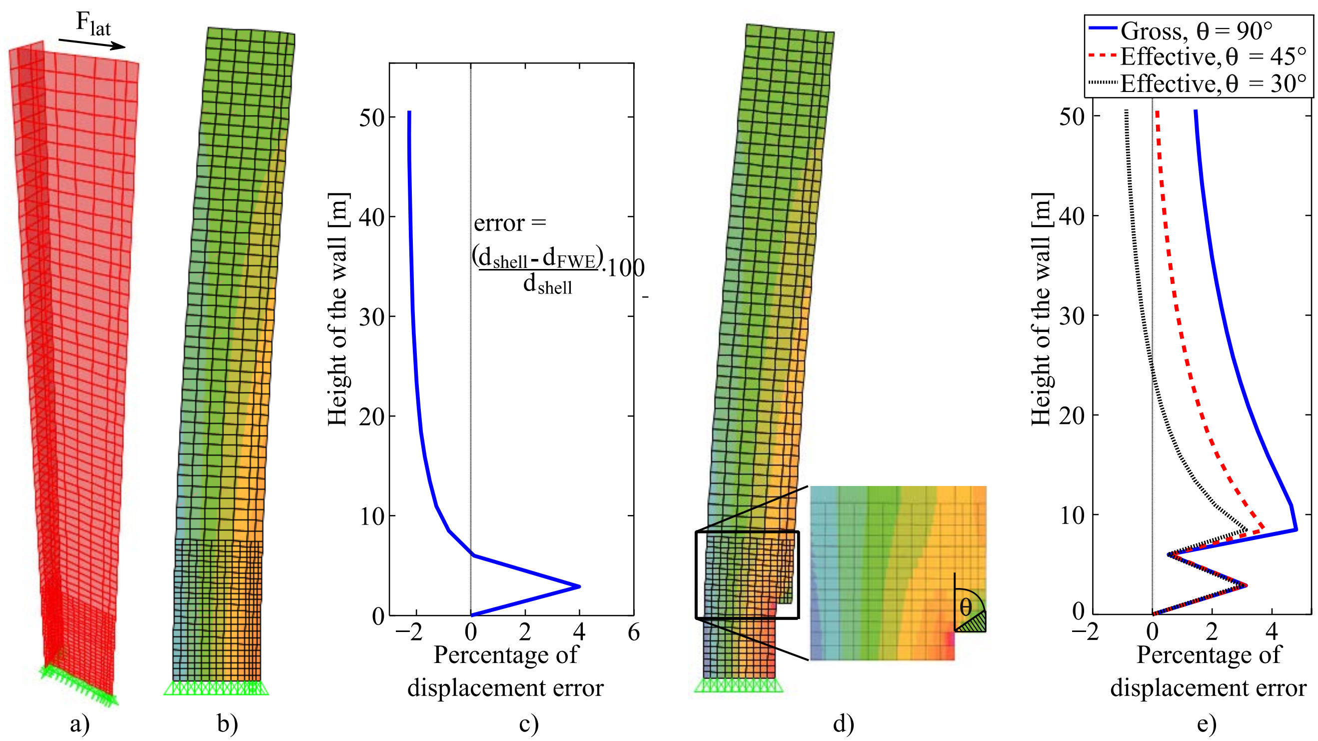

Fig. 7 – Comparison of linear elastic analysis using shell elements and FWE of a T-shaped wall shown in a). The shell analysis of the wall without irregularities in b), is compared to the analysis using several FWEs in c), while the shell analysis including the irregularity shown in d) is compared to the analysis with FWE using a variable effective wall length in the irregularity zone in e).

Finally, the wall with θ=30° was loaded with the lateral first mode shape of the building, and the vertical component was simply modeled as a constant total axial load of 19600 kN known from previous studies [25]. Due to the weight of a garden just above the irregularity, the axial load was not distributed equally on all stories. The story just below the irregularity had 491 kN more load than the others. Then, the critical zone had an ALR of 45% (the ALR at the base was 47.2%). The nonlinear material properties used were: concrete strength, $f_c' = 0.25ton/cm^2$, strain at this stress, $\varepsilon_0 = -0.002$, modulus of elasticity of steel, E_s =206010 MPa, yield stress F_{yield} =412 MPa, ultimate strain, $\varepsilon_u = 0.15$, buckling length of reinforcing bars, $L_{buckling}$ =0.2m, and concrete crushing energy $G_{crushing}$ =44 kN/m.

Figure 8 shows the graphical results of the simulated damage of the pushover. The color black indicates the largest deformation reached in the analysis, and the gray color indicates a deformation smaller than ε_0. It is apparent than the simulated failure is pretty similar to the actual one; it occurs at the same height and it tends to spread toward the opposite corner. The force-deformation state is shown for a roof displacement of 17.22 cm where the wall was not able to withstand the axial load. This was the end of the analysis, but it does not mean that the model can no longer predict what would have happened next under expected circumstances. This only means that the model cannot solve situations where the softening slope is vertical or even positive (snapback situation). In fact, a more appropriate load pattern is the use of vertical displacements, which actually result in variable axial loads, and after peak resistance, a decrease in axial loads is expected usually, which is exactly what happened in the pushover and dynamic analyses carried out elsewhere [25].

a)

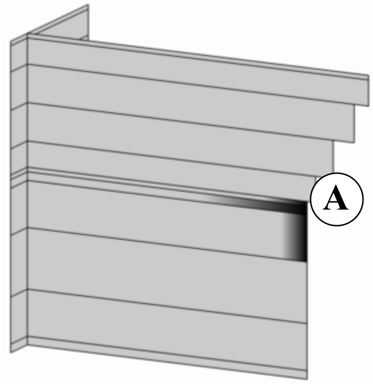

b)

Fig. 8 – Comparison of analytical an actual damage between: a) actual wall damage during the 2010, Chile earthquake, and b) simulated damage from a pushover analysis depicted as a function of strain. Black correspond to the most damaged zone

6. Conclusions

This article summarizes the formulation of a regularized fiber element to simulate the seismic behavior of reinforced concrete walls, additionally, the article summarizes the results of validation tests and applications. Special effort was placed in obtaining objective responses, which are mesh independent.

It is concluded that the proposed FWE is able to reproduce the extreme cyclic behavior of experimental rectangular and non-rectangular walls. Realistic nonlinear effects are accounted for such as softening of concrete, bar buckling, Bauschinger's effect, inelastic shear, and strain penetration effects. Additionally, the resulting FWE is mesh independent for a wide range of loading conditions thanks to the proposed regularization method.

The information regarding concrete and steel constitutive curves available in the literature is enough to accurately use the FWE, though calibration is needed for the steel if high tensile strains are expected. Therefore, the FWE is ready to be used in dynamic models of actual buildings. Common vertical irregularities can be modeled using a single element per story, and hence, the model should be able to provide accurate results at a rather low computational cost.

6. Acknowledgements

This research has been sponsored by the National Research Center for Integrated Natural Disaster Management CONICYT/FONDAP/15110017 and by Fondecyt grant #1141187.

7. References

[1] Wood S, Wight J, Moehle J (1987): The 1985 Chile earthquake: observations on earthquake-resistant construction in Viña del Mar. *Technical Report University of Illinois*, Champaign, USA.

[2] Jünemann R, de la Llera J, Hube M, Cifuentes L, Kausel E (2015): A statistical analysis of reinforced concrete wall buildings damaged during the 2010, Chile earthquake. *Engineering Structures*, **82**, 168–185.

[3] Song C, Pujol S, Lepage A. The Collapse of the Alto Río Building during the 27 February 2010 Maule, Chile, Earthquake (2012): *Earthquake Spectra*, **28** (S1), S301–S334.

[4] Petrangeli M, Pinto P, Ciampi V (1999): Fiber element for cyclic bending and shear of RC structures. I: Theory. *Journal of Engineering Mechanics*, **125** (9), 994–1001.

[5] Jiang H, Kurama Y (2010): Analytical modeling of medium-rise reinforced concrete shear walls. *ACI Structural Journal*, **107** (4), 400-410.

[6] Mullapudi R, Ayoub A (2009): Fiber beam element formulation using the Softened Membrane Model. *ACI Special Publication*, **265** (13), 283-300.

[7] Belmouden Y, Lestuzzi P (2007): Analytical model for predicting nonlinear reversed cyclic behaviour of reinforced concrete structural walls. *Engineering Structures*, **29** (7), 1263-1276.

[8] Marini A, Spacone E (2006): Analysis of reinforced concrete elements including shear effects. *ACI Structural Journal*, **103** (5), 645–655.

[9] Scott MH, Fenves GL (2006): Plastic Hinge Integration Methods for Force-Based Beam–Column Elements. *Journal of Structural Engineering*, **132** (2), 244–252.

[10] Almeida JP, Das S, Pinho R (2012): Adaptive force-based frame element for regularized softening response. *Computers & Structures*, **102**, 1-13.

[11] Coleman J, Spacone E (2001): Localization issues in force-based frame elements. *Journal of Structural Engineering*, **127** (11), 1257-1265.

[12] Pugh JS, Lowes LN, Lehman DE (2014): Seismic Design of slender concrete walls. *Tenth U.S. National Conference on Earthquake Engineering Frontiers*.

[13] Vásquez JA, de la Llera JC, Hube MA (2016): A regularized fiber element model for reinforced concrete shear walls. *Earthquake Engineering & Structural Dynamics*, **45** (13), 2063-2083.

[14] Spacone E, Filippou FC, Taucer FF (1996): Fibre Beam-Column Model for Non-Linear Analysis of R/C Frames: Part I. Formulation. *Earthquake Engineering & Structural Dynamics*, **25** (7), 711-725.

[15] Dhakal R, Maekawa K (2002): Path-dependent cyclic stress–strain relationship of reinforcing bar including buckling. *Engineering Structures*, **24** (11), 1383-1396.

[16] Calabrese A, Almeida JP, Pinho R (2010): Numerical Issues in Distributed Inelasticity Modeling of RC Frame Elements for Seismic Analysis. *Journal of Earthquake Engineering*, **14** (S1), 38-68.

[17] Pegon P, Plumier C, Pinto A, Molina J, Gonzalez P, Tognoli P, Olivier H (2000): U-shaped Walls: Quasi-static Test in the Y Direction: Test Report. *Technical Report no. I. European Commission, JRC Special Publication No.I.00.143*, Ispra, Italy.

[18] Brueggen BL (2009): Performance of T-shaped reinforced concrete structural walls under multi-directional loading. *PhD Thesis*, University of Minnesota, USA.

[19] Dazio A, Beyer K, Bachmann H (2009): Quasi-static cyclic tests and plastic hinge analysis of RC structural walls. *Engineering Structures*, **31** (7), 1556-1571.

[20] Scott B, Park R, Priestley M (1982): Stress-strain behavior of concrete confined by overlapping hoops at low and high strain rates. *ACI Journal*, **79** (1), 13-27.

[21] Légeron F, Paultre P (2003): Uniaxial confinement model for normal-and high-strength concrete columns. *Journal of Structural Engineering*, **129** (2), 241-252.

[22] Nakamura H, Higai T (2001): Compressive fracture energy and fracture zone length of concrete. *Modeling of inelastic behavior of RC structures under seismic loads*, 471–487.

[23] Zhao J, Sritharan S (2007): Modeling of strain penetration effects in fiber-based analysis of reinforced concrete structures. *ACI Structural Journal*, 104 (2), 133-141.

[24] Hassan M, El-Tawil S (2003): Tension Flange Effective Width in Reinforced Concrete Shear Walls: *ACI Structural Journal*, 100 (3), 349-356.

[25] Jünemann R, de la Llera JC, Hube MA, Vásquez JA, Chacón MF (2016): Study of the damage of reinforced concrete shear walls during the 2010 Chile earthquake. *Earthquake Engineering & Structural Dynamics*, **45** (10), 1621-1641.